Rayleigh–Taylor mixing rates for compressible flow

H. Jin, X. F. Liu, and T. Lu
*Department of Applied Mathematics and Statistics, Stony Brook University,
Stony Brook, New York 11794-3600*

B. Cheng
Applied Physics Division, Los Alamos National Laboratory, Los Alamos, New Mexico 87545

J. Glimm
*Department of Applied Mathematics and Statistics, Stony Brook University,
Stony Brook, New York 11794-3600 and Center for Data Intensive Computing,
Brookhaven National Laboratory, Upton, New York 11793-6000*

D. H. Sharp
*Applied Physics Division and Theoretical Division, Los Alamos National Laboratory,
Los Alamos, New Mexico 87545*

We study Rayleigh–Taylor instability in both the moderately compressible and weakly compressible regimes. For the two-dimensional single mode case, we find that the dimensionless terminal velocities (and associated Froude numbers) are nearly constant over most of this region of parameter space, as the thermodynamic parameters describing the equation of state are varied. The phenomenological drag coefficient which occurs in the single mode buoyancy-drag equation is directly related to the terminal velocities and has a similar behavior. Pressure differences and interface shape, however, display significant dependence on the equation of state parameters even for the weakly compressible flows. For three-dimensional multimode mixing, we expect accordingly that density stratification rather than drag will provide the leading compressibility effect. We develop an analytical model to account for density stratification effects in multimode self-similar mixing. Our theory is consistent with and extends numerically based conclusions developed earlier which also identify density stratification as the dominant compressibility effect for multimode three-dimensional mixing. © *2005 American Institute of Physics*. [DOI: 10.1063/1.1843155]

I. INTRODUCTION

Among the classic instabilities of a fluid interface, the Rayleigh–Taylor (RT) instability associated with steady acceleration has been studied for over four decades.[1] RT is important for astrophysics (supernova), geophysics (thunderstorms, saltdomes), and technology (inertially confined fusion) among other problems.

We examine first the well studied case of a single mode RT instability, i.e., a periodic array of identical modes, consisting of bubbles of light fluid rising into the heavy fluid and spikes falling into light fluid, under gravitational acceleration of an initially unstable (heavy over light) configuration. The modes grow initially at an exponential rate but eventually saturate, and achieve a terminal velocity

$$|V_{b,s}^{\infty}| = C_{b,s}\sqrt{Ag\lambda}, \tag{1}$$

with an Atwood number $A = (\rho_2 - \rho_1)/(\rho_2 + \rho_1)$ expressing the contrast in fluid densities between $\rho_1 = \rho_{\text{light}}$ and $\rho_2 = \rho_{\text{heavy}}$, $g = g(t)$ the gravitational acceleration, and λ the width of the periodic channel. Here the subscript "b" denotes bubble (light fluid penetrating into heavy fluid) and "s" denotes spike. $C_{b,s}^2$ is called the Froude number and it has been studied theoretically[2–4] and numerically.[5] For bubbles, it has the values $C_b = 0.23$ in two dimensions and $C_b = 0.34$ in three dimensions for $A = 1$ according to analytic theories[2–4] con-

firmed by experiment and two-dimensional (2D) simulations.[6] Alternate forms of (1) have been proposed[7] with A replaced by $2A/(A \pm 1)$,

$$|V_{b,s}^{\infty}| = C_{b,s}'\sqrt{\frac{2Ag\lambda}{A \pm 1}}, \quad C_{b,s}' = C_{b,s}\sqrt{\frac{A \pm 1}{2}}. \tag{2}$$

A more fundamental finite A theory for $C_{b,s}$ with a more complicated A dependence has been presented recently.[8,9] A correction to this basic picture was identified as a late time oscillation in $V_{b,s}$ about some mean value.[10] Moreover, the $A = 1$ Froude number in 3D depends on the planar symmetry group of the periodic bubbles[11,12] and this effect should hold for $A < 1$ also.

We discuss compressibility effects in RT mixing. We show in Sec. II that bubble and spike terminal velocities, i.e., the $C_{b,s}$ and the related single mode drag coefficients introduced below are relatively insensitive to compressible equation of state (EOS) parameters over the range of parameters we examine, for moderately compressible and nearly incompressible flows. However, detailed examination of the interface shapes and of the pressure differences between the heavy and light fluids, averaged at a common height, shows a strong dependence on EOS parameters. Thus convergence to a unique incompressible limit is not achieved within the very slightly compressible flows considered here.

17, 024104-1

We measure compressibility through the pseudo-Mach number

$$M_i = \frac{\sqrt{g\lambda}}{c_i}, \tag{3}$$

where c_i is the sound speed in fluid i. In view of (1),

$$M_i = \frac{1}{C_{b,s}\sqrt{A}} \times \text{Mach number} \tag{4}$$

is approximately five times the Mach number ($|V_{b,s}^\infty|/c_i$) of the bubble or spike tip at its terminal velocity for the value of $A = 1/3$ considered here. The dimensionless parameters governing compressible single mode RT mixing are M_i, A, and the EOS.

The complete EOS of a compressible fluid contains an infinite number of parameters. These should become irrelevant in the limit $M_i^2 \to 0$. For simplicity, we consider a simple model for the EOS, the stiffened γ-law gas, defined by the incomplete EOS

$$\rho c^2 = \gamma(p + P_\infty), \tag{5}$$

where P_∞ is a constant with the dimension of pressure. The RT instability with this EOS depends on four thermodynamic parameters, γ_1, γ_2, $P_{1\infty}$, and $P_{2\infty}$, as well as the flow parameters A and M_2 (M_1 is determined from M_2 and the thermodynamics). M_i^2 can also be understood as giving a length scale (in units of λ) over which compression induced density changes occur. Hydrostatic equilibrium is defined as a solution of the static momentum equation

$$\frac{dp}{dz} = \rho g. \tag{6}$$

The dependence of ρ (and thus p) on z can be specified initially by an arbitrary function of z.

Two natural choices for this initial $\rho(z)$ are defined by isothermal or isentropic thermodynamics. Assuming an isothermal initialization and a stiffened γ-law gas, the sound speeds are initially constant in each fluid and the density satisfies

$$\frac{d\rho}{dz} = \frac{\gamma\rho g}{c^2}. \tag{7}$$

Equation (7) is integrated to yield

$$\rho_i(z) = \rho_i^0 \exp\left[\frac{\gamma_i g(z - z_{\text{int}})}{c_i^2}\right] = \rho_i^0 \exp\left[\frac{\gamma_i M_i^2(z - z_{\text{int}})}{\lambda}\right], \tag{8}$$

where z_{int} is the initial mean interface position and ρ_i^0 is the density of fluid i at $z = z_{\text{int}}$. For a bubble or spike penetrating into an isothermally stratified ambient fluid, we assume a common horizontally averaged pressure in the two fluids as a function of z and isentropic density stratification in the penetrating phase. Using the ambient pressure from (7) and (8), we derive the formula

$$\rho_i(z) = \rho_i^0 \left\{ \mathcal{T}_i^0 \exp\left[\frac{\gamma_{i'} M_{i'}^2(z - z_{\text{int}})}{\lambda}\right] - \mathcal{T}_i^0 + 1 \right\}^{1/\gamma_i}, \tag{9}$$

where

$$\mathcal{T}_i^0 = \frac{\gamma_i M_i^0 \rho_{i'}^0}{\gamma_{i'} M_{i'}^2 \rho_i^0} = \frac{P_0 + P_{i'\infty}}{P_0 + P_{i\infty}} = \frac{1}{\mathcal{T}_{i'}^0} \tag{10}$$

is the relative stiffness of two fluids, $p_i = p_{i'} = P_0$ is the single pressure at $z = z_{\text{int}}$, and the primed index i' denotes the fluid complementary to fluid i, i.e., $i' = 3 - i$. Notice that $\mathcal{T}_i^0 = 1$ in case $P_{i\infty} = P_{i'\infty}$.

The single mode RT simulations at terminal velocity are not affected by density stratification, but due to the much longer time and perturbation heights needed to achieve self-similarity for multimode RT flows, density stratification is a leading compressibility effect for multimode flows. The stratification is measured by a time and space dependent Atwood number. In Sec. III, we propose a simple physics model for this stratification. The ambient fluids are assumed (at $t = 0$) to be isothermal. The penetrating fluids are assumed to have a single pressure at the bubble and spike tips and to change isentropically as they are displayed from their $t = 0$ isothermal state. Then formulas (8) and (9) yield a model for $A = A_b(z,t)$ and $A = A_s(z,t)$ at the bubble and spike tips. These formulas are compared to direct simulation data. On the basis of Sec. II results, we assume that the drag coefficient is only weakly sensitive to compressibility. On the basis of these two assumptions, we examine the solutions of the buoyancy-drag equation to predict compressibility effects on multimode RT mixing rates. We find density stratification as the leading compressibility effect. These predictions are compared to direct numerical simulations.

II. SINGLE MODE MIXING RATES

A. Growth models

Multimode (chaotic) mixing rates are defined as solutions of the buoyancy-drag equation

$$(\rho_i + \kappa_i \rho_{i'})\frac{d^2 Z_i}{dt^2} = (\rho_i - \rho_{i'})g - (-1)^i \frac{C_i^{m,d}\rho_{i'}V_i^2}{|Z_i|}. \tag{11}$$

This equation describes the motion of the edges Z_i, $i = 1, 2$ (or b, s) of an acceleration driven mixing layer. Here κ_i is an added mass coefficient due to the existence of fluid i', and $C_i^{m,d}$ is a phenomenological multimode drag coefficient for the edge of fluid i.

For self-similar (multimode) incompressible flow, the bubble and the spike fronts grow with the acceleration scaling proportional to gt^2,

$$Z_i(t) = (-1)^i \alpha_i A g t^2. \tag{12}$$

The RT mixing rates α_i have been measured in experiments[13–20] and characterized by theories[7,21–23] and simulation studies.[24–26] The experiments, theories, and two simulations[27,28] show a bubble growth rate of roughly 0.06 ± 0.01 (i.e., in the range $0.05 \pm 0.005 - 0.063 \pm 0.007$); the other simulations[29–31] give α_1 of the order of 0.03. A detailed discussion of the values of α_1 can be found in Ref. 32. To
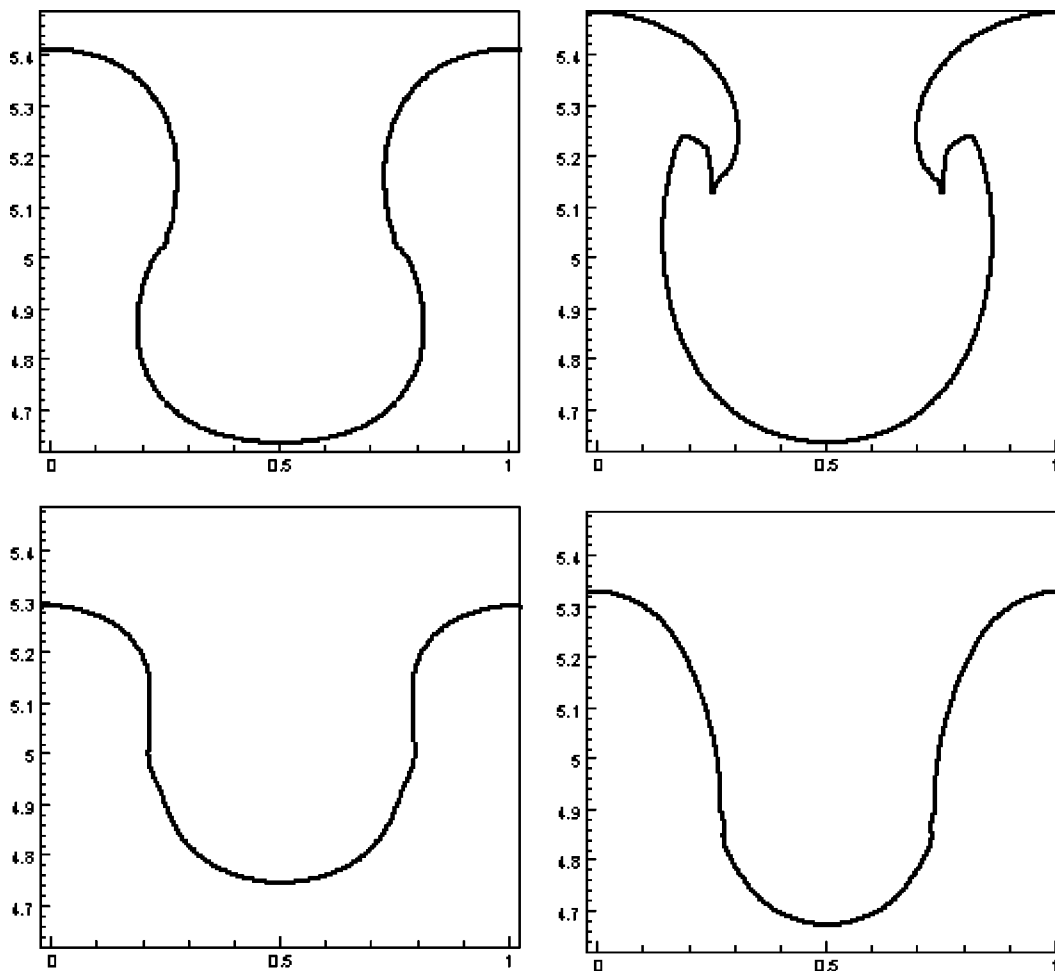
FIG. 1. The front plots at terminal velocity for the four cases in Table I. Here $M_2=0.05$. Gravity g points upward here, so that the bubble tip is located at the bottom of each figure.

this reference we add the comment that the value of α has been observed to or is believed to depend on surface tension (for immiscible fluids), physical or numerical mass diffusion (for miscible fluids), and on long wave length perturbations (noise) in the initial conditions, and for these reasons it may not be universal. At $A=1$, the spike rate $\alpha_2=1/2$. In this flow, the multimode drag coefficient $C_i^{m,d}=C_i^{m,d}(A)$ has the functional form[21]

$$C_i^{m,d}(A) = \frac{1/\alpha_i - [1+(-1)^iA] - \kappa_iL_i}{2L_i}, \tag{13}$$

where

$$L_i = 1 - (-1)^iA = \frac{2\rho_i}{\rho_1+\rho_2}. \tag{14}$$

We consider cylindrical compressible front bubbles and spikes ($\kappa_i \approx 1$).[21] For single mode RT mixing, $dV_i/dt=0$ at terminal velocity, $V_i=V_i^\infty$. We obtain

$$Ag = \frac{L_i}{2}\frac{C_i^{s,d}V_i^{\infty 2}}{\lambda} \tag{15}$$

from (11), where $C_i^{s,d}$ replaces $C_i^{m,d}$ as the single mode drag coefficient and $C_i^{s,d}$ is defined in terms of λ replacing $|Z_i|$ as

the drag length scale. From (15), we evaluate the terminal velocity

$$|V_i^\infty| = \sqrt{Ag\lambda} \times \sqrt{\frac{2}{L_iC_i^{s,d}}}. \tag{16}$$

The identity (16) shows the dependence of V_i^∞ on $2A/L_i$ $=2A/[1-(-1)^iA]$ as in (2). The comparison of (16) with (1) gives

$$C_{b,s} = \sqrt{\frac{2}{L_iC_i^{s,d}}}. \tag{17}$$

Using the value $C_b=0.23$ at $A=1$,[5] we get $C_1^{s,d}\simeq18.9$. Notice that the multimode drag coefficient is $C_1^{m,d}\simeq4.5$ by substitution of $\alpha_1\simeq0.05$ into (13). The drag coefficient of the single mode bubble front is approximately four times of that of the multimode bubble front. Therefore the single bubble terminal velocity is about half the multimode bubble front velocity, a result which is consistent with the numerical[33,34] and laboratory experiments. Physically, this is understandable because the merger process in multimode advances the bubble terminal velocity dramatically.

B. Compressible EOS effects

We show, through an extensive simulation study, that the drag coefficients $C_i^{s,d}$ and Froude numbers have small sensitivity to EOS parameters in the moderate to weak compressibility regime. In spite of this fact, we show striking EOS dependence even for very weakly compressible flows. The dependence is obvious in the shape of the interface at the time the terminal bubble velocity is achieved, see Fig. 1, and in the strong dependence of pressure differences (and pressure drag) on EOS parameters, both for weakly compressible flows.

We performed a systematic study of 2D Rayleigh–Taylor single mode instability simulations, using the front tracking code FronTier, with different EOS parameters as in (5). In our simulations, we set the Atwood number $A=1/3$. The initial configuration of the system contains a small amplitude, single sinusoidal mode interface with periodic boundary conditions on the left and right side of the computational domain of width λ. The top and bottom of the computational domain are Neumann boundaries. The initial amplitude of the perturbation is set to 0.015λ. The positions of the interfaces and the states of the system are updated by applying the front tracking method to the full two-dimensional Euler equations. All the numerical results use a 160×1600 grid in a 1×10 computational domain. It is known that the bubble velocity has gradual oscillations associated with gradual shape changes in the bubble and spike, after first reaching a maximum velocity,[8] so that the notion of terminal velocity for $A<1$ is not a precisely defined concept. We take the terminal velocity to be the velocity at the first maximum in these oscillations. We record the first peak as the terminal velocity, after which the velocity is weakly oscillatory as seen in Fig. 2. For the pressure differences and drag ratios (bubble or spike), $D_{b,s}^r=\{\text{pressure drag}\}/\{\text{form drag}\}$, there are rapid small oscillations at late time, removed by local time averages in Fig. 2.

Table I shows that the terminal velocity coefficients $C_{b,s}$ are nearly independent of EOS and compressibility parameters. See also Tables III–VI in the Appendix. From (17), the phenomenological drag coefficient $C_i^{s,d}$ in the single mode buoyancy-drag equation is related to the terminal velocities and it thus has a similar behavior. However, the solutions are not actually converging even within the fairly small Mach numbers we achieve with our compressible code. In Fig. 1, we observe that the shape of the bubble fronts at the terminal velocities depends significantly on the EOS parameters for very weakly compressible flows. Continuing this point of view, we see that pressure differences between the two phases are likewise sensitive to EOS and compressibility effects. The same sensitivity of pressure differences on simulation parameters was observed in Ref. 22 in the content of multiphase averaged equations.

Let Δp denote the difference p_2-p_1 in the pressures between the two phases, averaged over the horizontal space variable x, as a function of z and t. Then $\Delta p \leqslant 0$ at the bubble tip and $\Delta p \geqslant 0$ at the spike tip. We define $\Delta p_{b,s}$ to be the value of $(-1)^i\Delta p$ at the bubble or spike tip at the time of terminal velocity. Then $\Delta p_{b,s}/\lambda$ is a force, and it can be
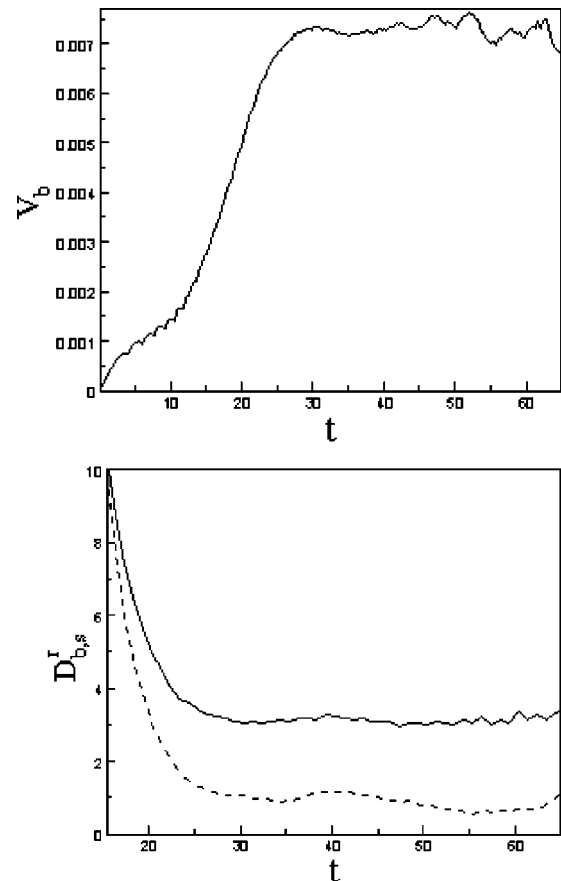

FIG. 2. Left, the bubble front velocity vs time. Right, convergence of the drag ratios $D_{b,s}^r$ to a large time asymptotic limit. Rapid small oscillations are suppressed by time averaging of the data. The top line (solid) is D_b^r and the bottom (dashed) is D_s^r. Here $M_2=0.05$, $P_{1\infty}/P_0=0$, $P_{2\infty}/P_0=10$, $\gamma_1=4.0$, and $\gamma_2=1.1$.

regarded as a pressure drag force on the bubble/spike tip. These forces display significant EOS and compressibility dependence in the moderate to weak compressibility regime. We dimensionalize this force through division by the form drag force or in view of (15) by Ag. Similar definitions apply to Δv and $\Delta v_{b,s}$. Here v_1 (v_2) is the light (heavy) phase velocity averaged over the x space.

Simple results in Table I and details in Tables III–VI in the Appendix show a significant dependence of the pressure drag force, or the drag ratio of EOS parameters and compressibility,

$$D_{b,s}^r = \frac{\Delta p_{b,s}}{\rho_{s,b}(\Delta v_{b,s})^2}. \tag{18}$$

The time dependent drag ratios are evaluated at the time of terminal (bubble or spike) velocity. The sensitivity of the drag ratios to EOS parameters results directly from the strong sensitivity of the pressure differences to these parameters. The strongest EOS dependence occurs in Table IV with $P_{1\infty}/P_0=10 \gg P_{2\infty}/P_0=0$ and for $\gamma_1=4.0 \gg \gamma_2=1.1$, which is in the four right columns of each table. Generally, the pressure differences and drag ratios decrease as the penetrating phase becomes stiffer (larger γ or P_∞) relative to the ambient phase, and these quantities are much more sensitive to varia-

TABLE I. Dependence of $C_{b,s}$ and drag ratio $D_{b,s}^r$ on compressible EOS parameters. Here P_0 is the pressure at the initial mean interface position. The smallest Mach numbers (the right most column) are ≈ 0.02. [See (3).]

EOS\M_2		0.55	0.32	0.1	0.05
$\gamma_1=2.0$, $\gamma_2=1.1$	M_1	0.29	0.17	0.05	0.03
$P_{1\infty}/P_0=P_{2\infty}/P_0=0$	C_b	0.31	0.30	0.25	0.25
	C_s	0.43	0.35	0.37	0.36
	D_b^r	1.1	1.2	1.9	2.0
	D_s^r	1.2	1.4	2.9	3.0
$\gamma_1=1.1$, $\gamma_2=2.0$	M_1	0.52	0.30	0.10	0.05
$P_{1\infty}/P_0=P_{2\infty}/P_0=10$	C_b	0.32	0.29	0.25	0.25
	C_s	0.41	0.43	0.39	0.40
	D_b^r	1.1	1.1	2.5	3.1
	D_s^r	1.0	1.0	1.5	1.9
$\gamma_1=4.0$, $\gamma_2=1.1$	M_1	0.68	0.39	0.12	0.06
$P_{1\infty}/P_0=0$, $P_{2\infty}/P_0=10$	C_b	0.29	0.32	0.26	0.25
	C_s	0.36	0.39	0.40	0.42
	D_b^r	1.0	1.2	2.5	3.1
	D_s^r	1.2	1.1	1.0	1.0
$\gamma_1=1.1$, $\gamma_2=4.0$	M_1	0.22	0.13	0.04	0.02
$P_{1\infty}/P_0=10$, $P_{2\infty}/P_0=0$	C_b	0.29	0.32	0.30	0.30
	C_s	0.43	0.43	0.40	0.39
	D_b^r	1.2	1.2	1.6	1.4
	D_s^r	1.1	1.6	3.1	3.6

tion of P_∞ than to variation of γ. We also observe that EOS effects are diminished at high compressibility, so that the $M_2=0.55$ column of Table I is nearly independent of the EOS, in contrast to the EOS dependence, especially of pressure differences and drag ratios for the weakly compressible column $M_2=0.05$. In the high compressibility limit, the pressure drag is approximately equal to the form drag.

C. Shape effects on compressible mixing rates

The purpose of this section is to study strong compressibility induced shape effects on mixing rates. We let compressibility M_2^2 vary from 0.1 to 0.8. Over this range, the terminal velocity increases by 10%. We study the radius of curvature and bubble width to understand compressibility induced shape effects. We calculate the radius curvature by fitting a circle to three interface points located at $x=0.45$, 0.5, and 0.55. We see from Table II a trend for the radius of curvature to increase as the compressibility increases. The

maximum bubble width follows the same trend. The minimum bubble width (which can be regarded as defining a maximum spike width) has an opposite trend and is probably not a good predictor of bubble motion. Shape is an important variable in determining drag and terminal velocity, as we see from Fig. 3 and the analysis here.

III. EFFECTS OF DENSITY VARIATION ON MIXING RATES

In this section, we study the effect of compressibility induced density stratification on 3D multimode mixing rates. The chaotic mixing problem differs from the single mode problem in that considerably longer solution times and penetration distances are needed to achieve asymptotic self-similar scaling. For this reason, density stratification associated with the weakly compressible regime is generally significant, in contrast to the single mode case where the flows have nearly constant density contrast. We develop an analytical model to account for density stratification effects in multimode self-similar mixing. From Ref. 25, we know that the compressible multimode simulations remain self-similar after removal of stratification effects, until a reversal of the Atwood number regime occurs. Here we reach the same conclusion through analytic models. We use the results of Sec. II to postulate that the multimode drag coefficients are not sensitive to weak or moderate compressibility effects and we study the influence of compressibility induced density stratification.
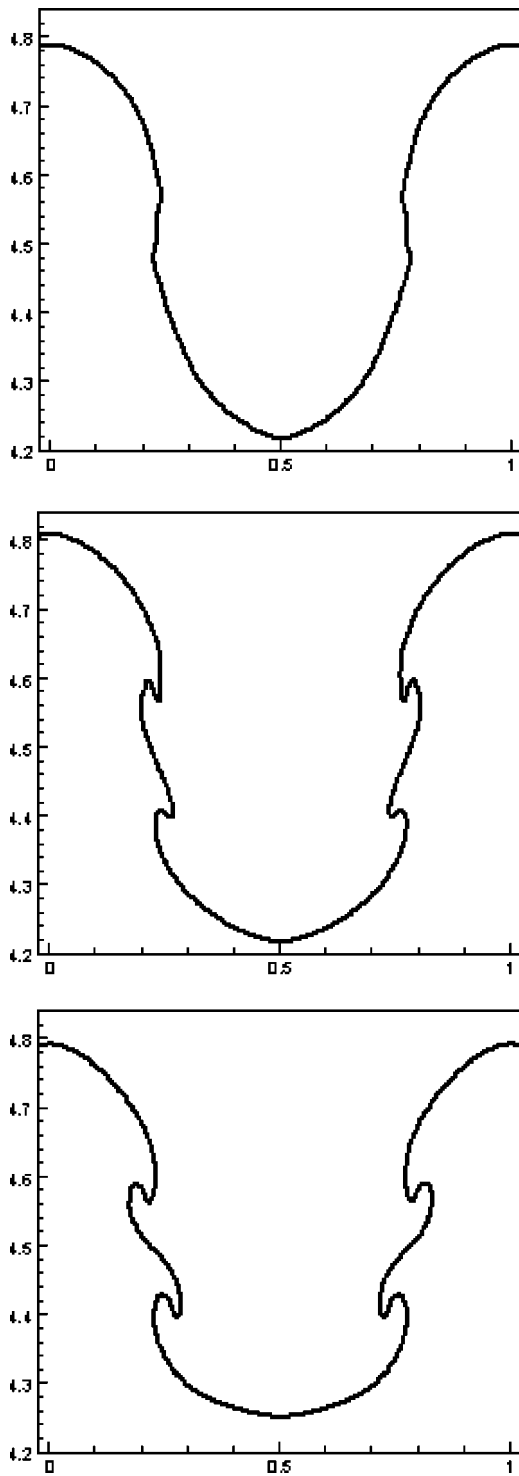
TABLE II. Radius curvature for the parameter values $A=1/3$, $\gamma_1=1.1$, $\gamma_2=4.0$, $P_{1\infty}/P_0=10$, and $P_{2\infty}/P_0=0$. Here $k=1/R$ is the bubble tip curvature.

M_2	C_b	$k=1/R$ at $V_b=V_b^\infty$	Bubble width (min)	Bubble width (max)
0.32	0.32	7.78	0.54	0.56
0.55	0.29	4.32	0.52	0.61
0.71	0.25	2.89	0.43	0.66
0.89	0.22	2.65	0.38	0.66

FIG. 3. 2D single mode RT front plots with different compressibilities (from left to right, $M_2 = 0.32, 0.55, 0.71$) at terminal velocity. Here γ_i and $P_{i\infty}$ are as in Table II.
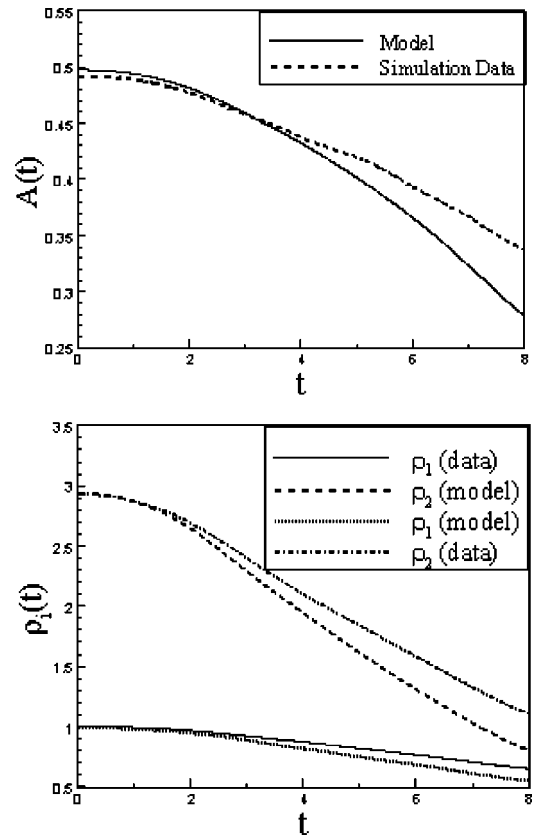

FIG. 4. Left, comparison of the model time dependent Atwood number $A_b(t)$ plotted vs time, with direct simulation data. Right, ρ_i at the bubble tip, comparing model, and simulation data. Here $M_2^2 = 0.1$ (moderately compressible).

where the multimode drag coefficient $C_i^{m,d}$ is given in (13) and L_i is defined in (14). Let $S_i = V_i^2/Z_i$. Then S_i can be regarded as a function of Z_i because $Z_i = Z_i(t)$ is monotone. We obtain
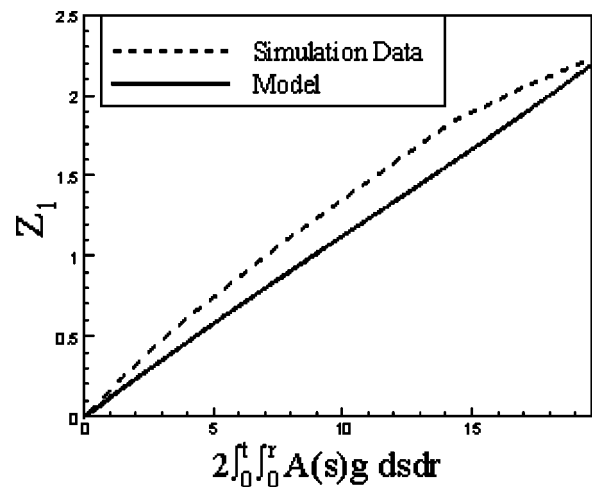

FIG. 5. Comparison of the model bubble edge with direct simulation data for the $M_2^2 = 0.1$ moderately compressible case. The dashed line represents the simulation data and the solid is calculated from the model Eqs. (19) and (24). The drag coefficient $C_1^{m,d}$ in (19) is chosen to allow approximate agreement between these curves.

For cylindrical front tips, we assume that $(-1)^i Z_i(t) > 0$ for $t > 0$, the initial mean interface height $Z_i(0) = 0$, and that the mixing zone expands, i.e., $(-1)^i V_i > 0$. Then Eq. (11) reduces to the equation

$$(-1)^i \ddot{Z}_i = Ag - (-1)^i \frac{L_i}{2} \frac{C_i^{m,d} V_i^2}{Z_i}, \tag{19}$$

TABLE III. $P_{1\infty}/P_0 = P_{2\infty}/P_0 = 0$.

$\gamma_2 \backslash \gamma_1$	$M_1, C_b, C_s, D_b^r, D_s^r$		
	1.1	2.0	4.0
1.1	0.07, 0.25, 0.39, 2.0, 2.0	0.05, 0.25, 0.37, 1.9, 2.9	0.04, 0.27, 0.35, 1.0, 4.0
2.0	0.10, 0.26, 0.40, 2.5, 1.5	0.07, 0.25, 0.39, 2.0, 2.0	0.05, 0.25, 0.37, 1.6, 3.0
4.0	0.13, 0.26, 0.42, 2.5, 1.0	0.10, 0.25, 0.40, 2.5, 1.5	0.07, 0.25, 0.39, 2.0, 2.0

$$\frac{dS_i}{dZ_i} = -\frac{V_i^2}{Z_i^2} + 2\frac{V_i}{Z_i}\frac{dV_i}{dZ_i}. \tag{20}$$

From (20), substitution of the identity $\ddot{Z}_i = dV_i/dt = V_i dV_i/dZ_i$ shows

$$Z_i\frac{dS_i}{dZ_i} = -S_i + 2\ddot{Z}_i. \tag{21}$$

Substituting (21) into (11), we obtain

$$(-1)^i\frac{1}{2}\left(Z_i\frac{dS_i}{dZ_i} + S_i\right) = Ag - (-1)^i\frac{L_i}{2}\mathcal{C}_i^{m,d}S_i, \tag{22}$$

i.e.,

$$(-1)^i Z_i\frac{dS_i}{dZ_i} = 2Ag - (-1)^i(L_i\mathcal{C}_i^{m,d} + 1)S_i. \tag{23}$$

We propose a physics model for time dependent Atwood number based on isothermal initial conditions. We assume isentropic flow within the mixing zone. The single phase region has very little flow so that its isothermal initialization property is retained. The density stratification thus satisfies (8) for the continuing phase flow at the mixing zone edge and (9) for the vanishing flow at the mixing zone edge. From (3), the phase i compressibility M_i is a dimensionless length-scale over which gravity causes significant fluid compression for fluid i. Motivated by Sec. II, we assume that the drag coefficient $\mathcal{C}_i^{m,d} = \mathcal{C}_i^{m,d}(A)$ is independent of M_i, and so we are concerned only with density stratification effects, i.e., variable Atwood number effects on the mixing rates. Then $\rho_i[\mathcal{T}_i^0\exp(\gamma_{i'}M_{i'}^2Z_i/\lambda) - \mathcal{T}_i^0 + 1]^{1/\gamma_i}$ will replace ρ_i and $\rho_{i'}\exp(\gamma_{i'}M_{i'}^2Z_i/\lambda)$ will replace $\rho_{i'}$ at the front tip Z_i in the drag-buoyancy equation. Thus only the Atwood number

$$A(Z_i) = (-1)^i\frac{\rho_i\left[\mathcal{T}_i^0\exp\left(\dfrac{\gamma_{i'}M_{i'}^2Z_i}{\lambda}\right) - \mathcal{T}_i^0 + 1\right]^{1/\gamma_i} - \rho_{i'}\exp\left(\dfrac{\gamma_{i'}M_{i'}^2Z_i}{\lambda}\right)}{\rho_i\left[\mathcal{T}_i^0\exp\left(\dfrac{\gamma_{i'}M_{i'}^2Z_i}{\lambda}\right) - \mathcal{T}_i^0 + 1\right]^{1/\gamma_i} + \rho_{i'}\exp\left(\dfrac{\gamma_{i'}M_{i'}^2Z_i}{\lambda}\right)} \tag{24}$$

at the bubble or spike tip in (23) changes, where $\mathcal{T}_i^0$ is defined in (10). In Fig. 4, we compare this model to numerical data from direct simulation of the multimode mixing.[25] The solid line in the left frame of Fig. 4 is the model Atwood number plot based on (24) using direct numerical simulation data Z_i. We see that the model is qualitatively correct but overstates the influence of density stratification. The differ-

ence between the model and the data is caused by two factors. Both heavy and light fluid at the bubble tip in the model are too light relative to the simulation data. The first, and larger, of these effects can be understood as follows. As confirmed from analysis of the 3D multimode simulation data,[25] some of the heavy fluid near the bubble tip originated near the $Z=0$ value for the initial bubble position and was trans-

TABLE IV. $P_{1\infty}/P_0 = P_{2\infty}/P_0 = 10$.

$\gamma_2 \backslash \gamma_1$	$M_1, C_b, C_s, D_b^r, D_s^r$		
	1.1	2.0	4.0
1.1	0.07, 0.25, 0.39, 2.0, 2.0	0.05, 0.25, 0.38, 1.8, 2.7	0.04, 0.26, 0.35, 1.0, 3.7
2.0	0.10, 0.25, 0.39, 2.5, 1.5	0.07, 0.25, 0.39, 2.0, 2.0	0.05, 0.25, 0.37, 1.6, 3.0
4.0	0.13, 0.26, 0.41, 2.5, 1.0	0.10, 0.26, 0.40, 2.5, 1.5	0.07, 0.25, 0.38, 2.1, 2.1

TABLE V. $P_{1\infty}/P_0=0$ and $P_{2\infty}/P_0=10$.

$\gamma_2 \backslash \gamma_1$	$M_1, C_b, C_s, D_b^r, D_s^r$		
	1.1	2.0	4.0
1.1	0.23, 0.26, 0.43, 2.5, 0.6	0.17, 0.26, 0.42, 2.5, 0.9	0.12, 0.26, 0.40, 2.5, 1.0
2.0	0.32, 0.26, 0.44, 2.5, 0.5	0.23, 0.26, 0.42, 2.5, 0.5	0.17, 0.26, 0.41, 2.5, 0.9
4.0	0.45, 0.26, 0.44, 2.5, 0.4	0.33, 0.26, 0.44, 2.5, 0.5	0.23, 0.27, 0.44, 2.5, 0.6

ported there by the bubble motion. This heavy fluid evolves from its $Z=0$ density isentropically and is heavier than the model assumption.

In Fig. 5, we compare the edge model (19) with the direct numerical data.[25] The solid line represents the solution $Z_1(t)$ of (19) with the Atwood number (24). Here the drag coefficient in (19) is an adjustable parameter, chosen to give the best fit for this comparison. We are here comparing not only the buoyancy-drag equation (19) to simulation, but also the influence of the model (24) or a time dependent Atwood number in this comparison.

The exact solution of (23) is

$$S_i = S_i^{(0)} \exp\left[-\int_0^{Z_i} \frac{L_i(y)\mathcal{C}_i^{m,d}+1}{y}dy\right]$$
$$+ \int_0^{Z_i} \exp\left[\int_{Z_i}^{y} \frac{L_i(s)\mathcal{C}_i^{m,d}+1}{s}ds\right]\frac{(-1)^i 2A(y)g}{y}dy, \tag{25}$$

where $S_i^{(0)} \equiv S_i(Z_i=0)$, $A(Z_i)$ is given in (24) and

$$L_i(Z_i) = 1 - (-1)^i A(Z_i). \tag{26}$$

From (23), we see that for a finite dS_i/dZ_i at $Z_i=0$, the initial condition is given as

$$S_i^{(0)} = S_i(Z_i=0) = (-1)^i \frac{2Ag}{L_i \mathcal{C}_i^{m,d}+1} = (-1)^i 4\alpha_i Ag, \tag{27}$$

where $A=A(Z_i=0)$ and $L_i=L_i(Z_i=0)$.

The integrals in (25) are not evaluated explicitly, so we introduce the approximation of (24),

$$A(Z_i) \approx A + (-1)^i \frac{(1-A^2)\gamma_{i'}M_{i'}^2(\mathcal{T}_i^0-\gamma_i)}{2\gamma_i \lambda}Z_i, \tag{28}$$

valid for small $\gamma_{i'}M_{i'}^2 Z_i/\gamma_i \lambda$, i.e., small Z_i and $M_{i'}$. Suppose that

$$S_i(Z_i) = S_i^{(0)} + S_i^{(1)} Z_i \tag{29}$$

for small Z_i. We substitute (28) and (29) into (23) and equate terms of the same order of Z_i. Notice that the zeroth-order terms cancel. Using (27), the coefficients of Z_i give the identity

$$S_i^{(1)} = \frac{g(\mathcal{C}_i^{m,d}+1)(1-A^2)\gamma_{i'}M_{i'}^2(\mathcal{T}_i^0-\gamma_i)}{\gamma_i \lambda(L_i \mathcal{C}_i^{m,d}+2)(L_i \mathcal{C}_i^{m,d}+1)}. \tag{30}$$

Observe that the sign of $S_i^{(1)}$ depends on the sign of $\mathcal{T}_i^0-\gamma_i$. We note that if $A=1$ or $\mathcal{T}_i^0=\gamma_i$ is satisfied, it follows from (30) that $S_i^{(1)}=0$ and thus a higher order approximation is required for $S_i=S_i(Z_i)$ in (29). Assuming that $S_i^{(1)}\neq 0$, we now solve the equation

$$\frac{V_i^2}{Z_i} = S_i^{(0)} + S_i^{(1)} Z_i \tag{31}$$

for Z_i. The solution of Eq. (31) is

$$Z_i = \begin{cases} \frac{S_i^{(0)}}{2S_i^{(1)}}[\cosh(t\sqrt{S_i^{(1)}})-1] & \text{if } S_i^{(1)}>0 \\ \frac{S_i^{(0)}}{2S_i^{(1)}}[\cos(t\sqrt{-S_i^{(1)}})-1] & \text{if } S_i^{(1)}<0 \end{cases}. \tag{32}$$

From (32), we derive for small $t\sqrt{|S_i^{(1)}|}$,

$$Z_i = \frac{t^2 S_i^{(0)}}{4}\left[1 + \frac{t^2 S_i^{(1)}}{12} + O(t^4 S_i^{(1)2})\right]. \tag{33}$$

This holds for small $t^2|S_i^{(1)}|$, i.e.,

$$t^2 \frac{g(1-A^2)\gamma_{i'}M_{i'}^2|\mathcal{T}_i^0-\gamma_i|}{\gamma_i \lambda} \ll 1. \tag{34}$$

In the incompressible limit, $M_i=0$ and $S_i^{(1)}=0$, Eq. (33) gives the asymptotic solution $Z_i=t^2 S_i^{(0)}/4$ which recovers the incompressible flow solution (12).

TABLE VI. $P_{1\infty}/P_0=10$ and $P_{2\infty}/P_0=0$.

$\gamma_2 \backslash \gamma_1$	$M_1, C_b, C_s, D_b^r, D_s^r$		
	1.1	2.0	4.0
1.1	0.02, 0.36, 0.39, 0.7, 5.2	0.016, 0.40, 0.40, 0.5, 4.9	0.01, 0.49, 0.40, 0.02, 6.8
2.0	0.03, 0.33, 0.40, 1.1, 4.0	0.02, 0.36, 0.40, 0.6, 5.0	0.015, 0.43, 0.40, 0.2, 6.0
4.0	0.04, 0.30, 0.40, 1.6, 3.1	0.03, 0.32, 0.39, 1.0, 3.5	0.02, 0.37, 0.39, 0.5, 5.4

In general, when the ambient fluid is relatively stiffer, then compressibility speeds up the mixing of the penetrating (less stiff) fluid. We classify the relative stiffness of the light and the heavy fluids into three cases when $A \neq 1$ and $\mathcal{T}_i^0 \neq \gamma_i$. Note $\gamma_{i'}^{-1} < 1 < \gamma_i$ always and $\mathcal{T}_1^0 \mathcal{T}_2^0 = 1$ in view of (10).

Case 1. Assume

$$\mathcal{T}_i^0 > \gamma_1. \qquad (35)$$

This case occurs when the heavy fluid is stiffer than the light fluid. From (30), we see that $S_1^{(1)} > 0$ and $S_2^{(1)} < 0$. Thus, (33) implies that compressibility makes the bubble edge of the mixing zone grow faster while the spike edge is slower.

Case 2. Assume

$$\gamma_2^{-1} < \mathcal{T}_i^0 < \gamma_1. \qquad (36)$$

The two fluids are of comparable stiffness. For example, the case $P_{1\infty} = P_{2\infty}$ falls into this category. In this case, $S_1^{(1)} < 0$ and $S_2^{(1)} < 0$, so both the bubble and the spike grow more slowly when compressibility is included in the buoyancy-drag equation.

Case 3. Assume

$$\mathcal{T}_1^0 < \gamma_2^{-1}. \qquad (37)$$

This case occurs when the light fluid is stiffer than the heavy fluid. We obtain $S_1^{(1)} < 0$ and $S_2^{(1)} > 0$ from (30). Therefore compressibility makes the spike edge grow faster while the bubble edge is slower.

The results are valid for small $t\sqrt{|S_i^{(1)}|}$, i.e., when (34) holds. Numerical simulations of (11) (not reported here) show that these early time trends are preserved into later time.

IV. CONCLUSIONS

We find insensitivity of Froude numbers and drag coefficients to compressibility and EOS parameters, but in contrast a strong dependence of shape and pressure differences on these same qualities. For multimode mixing, the dominant compressibility effect is due to compressibility induced density stratification of the fluids.

ACKNOWLEDGMENTS

APPENDIX: EOS DEPENDENCE OF THE FROUDE NUMBER AND DRAG RATIO IN THE WEAKLY COMPRESSIBLE LIMIT

In Tables III–VI we show that dependence of $C_{b,s}$ and the drag ratio $D_{b,s}^r$ on the EOS. Here $M_2 = 0.1$ and P_0 is the pressure at the initial mean interface position.

[1] D. H. Sharp, "An overview of Rayleigh-Taylor instability," Physica D **12**, 3 (1984).

[2] G. Birkhoff and D. Carter, "Rising plane bubbles," J. Math. Mech. **6**, 769 (1957).

[3] P. Garabedian, "On steady-state bubbles generated by Taylor instability," Proc. R. Soc. London, Ser. A **241**, 423 (1957).

[4] D. Layzer, "On the instability of superimposed fluids in a gravitational field," Astrophys. J. **122**, 1 (1955).

[5] Q. Zhang, "The motion of single bubble or spike in Rayleigh-Taylor unstable interfaces," Impact Comput. Sci. Eng. **3**, 277 (1991).

[6] R. Menikoff and C. Zemach, "Rayleigh-Taylor instability and use of conformal maps for ideal fluid flow," J. Comput. Phys. **51**, 28 (1983).

[7] D. Oron, L. Arazi, D. Kartoon, A. Rikanati, U. Alon, and D. Shvarts, "Dimensionality dependence of the Rayleigh-Taylor and Richtmyer-Meshkov instability late-time scaling laws," Phys. Plasmas **8**, 2883 (2001).

[8] S. I. Abarzhi, J. Glimm, and A.-D. Lin, "Rayleigh-Taylor instability for fluids with a finite density contrast," Phys. Fluids **15**, 2190 (2003).

[9] S. I. Abarzhi, J. Glimm, and K. Nishihara, "Rayleigh-Taylor instability and Richtmyer-Meshkov instabilities for fluids with a finite density contrast," Phys. Lett. A **11**, 1 (2003).

[10] J. Glimm, X.-L. Li, and A.-D. Lin, "Nonuniform approach to terminal velocity for single mode Rayleigh-Taylor instability," Acta Math. Appl. Sin. **18**, 1 (2002).

[11] S. Abarzhi and A. Oparin, "Three-dimensional bubbles in Rayleigh-Taylor instability," Phys. Fluids **11**, 3306 (1999).

[12] S. I. Abarzhi, "Bubble symmetry in the Rayleigh-Taylor instability," Phys. Scr. **56**, 296 (1999).

[13] G. Dimonte, "Nonlinear evolution of the Rayleigh-Taylor and Richtmyer-Meshkov instabilities," Phys. Plasmas **6**, 2009 (1999).

[14] G. Dimonte and M. Schneider, "Turbulent Rayleigh-Taylor instability experiments with variable acceleration," Phys. Rev. E **54**, 3740 (1996).

[15] G. Dimonte and M. Schneider, "Density ratio dependence of Rayleigh-Taylor mixing for sustained and impulsive acceleration histories," Phys. Fluids **12**, 304 (2000).

[16] D. L. Youngs, "Modeling turbulent mixing by Rayleigh-Taylor instability," Physica D **37**, 270 (1989).

[17] K. I. Read, "Experimental investigation of turbulent mixing by Rayleigh-Taylor instability," Physica D **12**, 45 (1984).

[18] Yu. A. Kucherenko, L. I. Shibarshev, V. I. Chitaikin, S. A. Balabin, and A. P. Palaev, "Experimental study of the gravitational turbulent mixing self-similar mode," *Proceedings of the third International Workshop on Physics Compressible Turbulent Mixing*, edited by R. Dautray (Commissariat Energie Atomique, Cesta, France, 1991), p. 427.

[19] A. M. Vasilenko, V. I. Olhovskaya, O. V. Buryakov, and V. G. Yakovlev, "Experimental investigations for turbulent mixing of gases at the plane interface under the influence of the decelerating shock wave," *Proceedings of the third International Workshop on Physics Compressible Turbulent Mixing*, edited by R. Dautray (Commissariat Energie Atomique, Cesta, France, 1991), pp. 535–552.

[20] E. E. Meshkov and N. V. Neumerzhisky, "About trubulent mixing dynamics at unstable boundary of liquid layer, accelerated by compressed gas," *Proceedings of the third International Workshop on Physics Compressible Turbulent Mixing*, edited by R. Dautray (Commissariat Energie Atomique, Cesta, France, 1991), pp. 467–476.

[21] B. Cheng, J. Glimm, and D. H. Sharp, "Density dependence of Rayleigh-Taylor and Richtmyer-Meshkov mixing fronts," Phys. Lett. A **268**, 366 (2000).

[22] B. Cheng, J. Glimm, and D. H. Sharp, "A three-dimensional renormalization group bubble merger model for Rayleigh-Taylor mixing," Chaos **12**, 267 (2002).

[23] B. Cheng, J. Glimm, and D. H. Sharp, "Dynamical evolution of the Rayleigh-Taylor and Richtmyer-Meshkov mixing fronts," Phys. Rev. E **66**, 036312 (2002).

[24] B. Cheng, J. Glimm, X. L. Li, and D. H. Sharp, "Subgrid models and DNS studies of fluid mixing," *Proceedings of the Seventh International Conference on the Physics of Compressible Turbulent Mixing, 1999*, edited by E. Meshkov, Y. Yanilkin, and V. Zhmailo (Nizhny Novgorod, Sarov, Russia, 2001), pp. 385–390.

[25] E. George and J. Glimm, "Self similarity of Rayleigh-Taylor mixing rates," Phys. Fluids (submitted).

[26] E. George, J. Glimm, X. L. Li, A. Marchese, and Z. L. Xu, "A comparison of experimental, theoretical, and numerical simulation Rayleigh-Taylor mixing rates," Proc. Natl. Acad. Sci. U.S.A. **99**, 2587 (2002).

[27] J. Glimm, J. Grove, X. L. Li, W. Oh, and D. Sharp, "A critical analysis of Rayleigh-Taylor growth rates," J. Comput. Phys. **69**, 652 (2001).

[28] K. Kadau, T. C. Germann, N. G. Hadjiconstantinou, P. S. Lomdahl, G.

Dimonte, B. L. Holian, and B. J. Alder, "Nanohydrodynamics simulations: An atomistic view of the Rayleigh-Taylor instability," Proc. Natl. Acad. Sci. U.S.A. **101**, 5851 (2004).

[29] D. L. Youngs, "Three dimensional numerical simulation of turbulent mixing by Rayleigh-Taylor instability," Phys. Fluids A **3**, 1312 (1991).

[30] A. W. Cook and P. E. Dimotakis, "Transitional stages of Rayleigh-Taylor instability," J. Fluid Mech. **443**, 69 (2001).

[31] Y. N. Youngs, H. Tofo, A. Dubey, and R. Rosner, "On the miscible Rayleigh-Taylor instability: Two and three dimensions," J. Fluid Mech. **447**, 377 (2001).

[32] G. Dimonte, D. L. Youngs, A. Dimits, S. Weber, M. Marinak, S. Wunsch, C. Garasi, A. Robinson, M. Andrews, P. Ramaprabhu, A. C. Calder, B. Fryxell, J. Bielle, L. Dursi, P. MacNeice, K. Olson, P. Ricker, R. Rosner, F. Timmes, H. Tubo, Y.-N. Young, and M. Zingale, "A comparative study of the turbulent Rayleigh-Taylor instability using high-resolution three-dimensional numerical simulations: The Alpha-Group collaboration," Phys. Fluids **16**, 1668 (2004).

[33] J. Glimm, X.-L. Li, R. Menikoff, D. H. Sharp, and Q. Zhang, "A numerical study of bubble interactions in Rayleigh-Taylor instability for compressible fluids," Phys. Fluids A **2**, 2046 (1990).

[34] J. Glimm and X.-L. Li, "On the validation of the Sharp-Wheeler bubble merger model from experimental and computational data," Phys. Fluids **31**, 2077 (1988).